INTERFACE

rsif.royalsocietypublishing.org

Research

Cite this article: Kundanati L, Signetti S, Gupta HS, Menegon M, Pugno NM. 2018 Multilayer stag beetle elytra perform better under external loading via non-symmetric bending properties. *J. R. Soc. Interface* **15**: 20180427.
http://dx.doi.org/10.1098/rsif.2018.0427

Received: 9 June 2018
Accepted: 25 June 2018

Subject Category:
Life Sciences – Engineering interface

Subject Areas:
biomechanics

Keywords:
elytra, multilayer, asymmetric bending, modelling

Author for correspondence:
Nicola M. Pugno
e-mail: nicola.pugno@unitn.it

†Present address: Department of Mechanical Engineering, Korea Advanced Institute of Science and Technology (KAIST), 291 Daehak-ro, Yuseong-gu, Daejeon 34141, Republic of Korea.

Electronic supplementary material is available online at https://dx.doi.org/10.6084/m9.figshare.c.4150937.

THE ROYAL SOCIETY PUBLISHING

Multilayer stag beetle elytra perform better under external loading via non-symmetric bending properties

Lakshminath Kundanati[1], Stefano Signetti[1,†], Himadri S. Gupta[2], Michele Menegon[3] and Nicola M. Pugno[1,2,4]

[1]Laboratory of Bio-inspired and Graphene Nanomechanics, Department of Civil, Environmental and Mechanical Engineering, University of Trento, via Mesiano 77, 38123 Trento, Italy
[2]School of Engineering and Materials Science, Queen Mary University of London, Mile End Road, London E1 4NS, UK
[3]MUSE Science Museum, corso del Lavoro e della Scienza 3, 38122 Trento, Italy
[4]Ket-Lab, Edoardo Amaldi Foundation, Italian Space Agency, Via del Politecnico snc, 00133 Roma, Italy

LK, 0000-0003-3997-9415; SS, 0000-0003-4128-0953; HSG, 0000-0003-2201-8933; NMP, 0000-0003-2136-2396

Insect cuticle has drawn a lot of attention from engineers because of its multifunctional role in the life of insects. Some of these cuticles have an optimal combination of lightweight and good mechanical properties, and have inspired the design of composites with novel microstructures. Among these, beetle elytra have been explored extensively for their multilayered structure, multifunctional roles and mechanical properties. In this study, we investigated the bending properties of elytra by simulating their natural loading condition and comparing it with other loading configurations. Further, we examined the properties of their constitutive bulk layers to understand the contribution of each one to the overall mechanical behaviour. Our results showed that elytra are graded, multilayered composite structures that perform better in natural loading direction in terms of both flexural modulus and strength which is likely an adaptation to withstand loads encountered in the habitat. Experiments are supported by analytical calculations and finite element method modelling, which highlighted the additional role of the relatively stiff external exocuticle and of the flexible thin bottom layer in enhancing flexural mechanical properties. Such studies contribute to the knowledge of the mechanical behaviour of this natural composite material and to the development of novel bioinspired multifunctional composites and for optimized armours.

1. Background

Insect cuticle is a biological structure that has been widely investigated for its microstructure because of its crucial role in providing protection and simultaneously permitting locomotion. The composite nature and complex structural design of cuticle determine its mechanical response in terms of strength, bending stiffness, toughness and wear resistance [1]. Insect cuticles are natural fibre-layered composites primarily made of chitin microfibrils and protein, with layers of varying thickness and fibre alignment [2]. The variation in cuticle properties across species is achieved by changing composition, fibre density and orientation, and cross-linking of the protein matrix [3]. Insect cuticle comprises three layers and the outermost epicuticle is a thin wax layer [4]. The other two layers comprise chitin microfibrils embedded in a protein matrix. One of them is the exocuticle which is hardened by sclerotization process [5], and the other is the unsclerotized endocuticle that is tougher and more flexible [6]. Recent studies have reported on how multi-scale elastic gradients in cuticle-based organs like spider fangs enhance their biomechanical functionality [7]. Such structural gradients were also observed in the tarsal

setae of seven-spot ladybird (*Coccinella septempunctata*), which enable contact formation with substrates on which they walk and prevent condensation, resulting in increased pad attachment [8].

Elytra are a variation of beetle cuticle with a dorsal layer and a ventral layer, which are connected by a haemolymph space and columnar trabecular structures [9]. The mechanical interaction between various bulk layers and the constitutive sublayers together determines the structural performance of the whole elytron. Also, the progressive fibre arrangement in each sublayer of elytra has been shown to be crucial to mechanical performance [9], while the presence of trabecular structures was hypothesized for energy absorbing function [10]. Elytra have drawn a lot of attention because of their light weight in combination with excellent Young's modulus and hardness, and their peculiar surface texturing resulting in specific optical properties and hydrophobicity [11,12]. Elytra play an important role in the survival of some beetles by shielding the insect from damage during battles. In addition, the interaction between the elytron and the flexible wing during flapping has been claimed to improve the aerodynamic force enough to compensate for the weight of the beetle during forward flight [13]. Thus, flexibility of the elytra also plays a role in dynamic interaction with the wind flow during the flight. Such studies based on elytron design led to the development of structural models [10] and novel biomimetic layered composites with specialized microstructures [14,15], and were also employed in building construction [16].

In this study, we chose male stag beetles (*Lucanus cervus*) because of their large size and their battle behaviour using large puncturing mandibles. Earlier studies on stag beetles were focused on determining bite forces of the mandible and modelling the bites during fights to understand the biomechanical aspects of their mandible movement and its properties [17]. In some instances, the elytron comes in contact with the mandible during battle and the elytron's bending response plays a crucial role in preventing damage. In principle, the elytra of beetles should be resistant to fracture and be rigid enough to sustain bending loads without internal damage to help in the beetle's survival. Overall, elytra play a multifunctional role in resisting wear from outside environment and protecting the fragile wings when they are folded. Most earlier studies dealing with elytra characterization primarily focused on tensile testing, on dynamic mechanical analysis and, in some cases, on nano-indentation [18–20]. Very few studies have explored the more physiologically relevant bending properties of elytra, which closely simulate natural loading scenario that a beetle experiences in its habitat. Thus, elytron with its multilayered complex microstructure requires a more detailed investigation of its multifunctional mechanical performance. The goal of our study is to provide comprehensive structural and mechanical characterization of the composite elytra in physiological deformation modes and also to investigate the contribution of each layer. Initially, tensile tests were performed on two sample sizes to examine the size effects in the elytra mechanical strength, followed by bending experiments. We then performed tensile tests on each layer to determine their material constitutive properties and to quantitatively assess their contribution to the overall mechanical behaviour. The determined layer properties were used to carry out analytical predictions of the overall bending behaviour of elytra and also as input for finite element method (FEM) simulation to better understand the deformation mechanisms, delamination and fracture behaviour of the multilayer composite structure. The understanding of the role of different layers with different mechanical properties and of the overall elytron structure in its deformation and fracture behaviour will also help in more detailed design of bioinspired lightweight composites and structures, e.g. for impact resistance in advanced applications.

2. Material and methods

2.1. Optical and electron microscopy

The male stag beetle specimens were acquired in dehydrated state from the collection of the MUSE Science Museum of Trento (Trento, Italy). Images of insects were captured using a camera (Sony HDR XR500) as shown in figure 1*a*. Scanning electron microscopy (SEM) imaging was performed directly on samples without any preparation because of the relative dryness of elytra samples. Prepared elytra sections from the dissection and mechanical tests were carefully mounted on double-sided carbon tape, stuck on an aluminium stub followed by sputter coating (Manual Sputter Coater, AGAR SCIENTIFIC) with gold. Imaging was carried out using an SEM (EVO 40 XVP, ZEISS, Germany) with accelerating voltages between 5 and 10 kV. ImageJ software was used for all dimensional quantification reported in this study [21].

2.2. Mechanical testing

Mechanical tests were performed on the sample sections (figure 1*b*), using a Messphysik MIDI 10 (MESSPHYSIK, Germany) universal testing machine and forces were obtained using transducers of two ranges (LEANE Corp., ± 10 N and METTLER TOLEDO, ± 200 N). In monotonic tension, specimens were tested in displacement control mode at a rate of 0.01 mm s^{-1}. Engineering stresses were calculated as ratio of applied load to the nominal specimen cross-sectional area. Axial strains were defined as ratio of change in displacement to initial specimen length. Tensile tests were performed on two sets of samples (three samples from mid location of elytra of each beetle as shown in figure 1*b*) with different sizes: large size samples (length $= 6.59 \pm 1.8$ mm, width $= 2.62 \pm 0.6$ mm) and small size samples (length $= 1.79 \pm 0.26$ mm, width $= 0.98 \pm 0.23$ mm).

Bending experiments were performed using the same machine with a custom built three-point bending set-up machined out of hard plastic material on which blunted blades are mounted to achieve line contact during loading. The rate of testing in three-point bending tests was 0.01 mm s^{-1}. In order to observe and ensure the tests were done without any significant slipping of the sample, all the mechanical tests were monitored using a video camera (Sony HDR XR500) with an objective lens (Olympus 1.5XPF) kept at a distance of approximately 5 cm from the samples. First set of bending tests (four samples in each direction, from four beetles) on elytra were performed from the hinge location to examine in-plane anisotropy at a given location in the longitudinal and transverse directions, orthogonal to each other, as shown in figure 1*b*. We then performed a second set of bending tests using samples from middle region of elytra to compare the response of elytra to opposite bending directions (three samples each from four beetles). In this study, the combined epicuticle and exocuticle layers are referred to as the top layer, the endocuticle is referred to as middle layer and the lower lamination is referred to as bottom layer, which is the thinnest of all layers (figure 1*c*). The

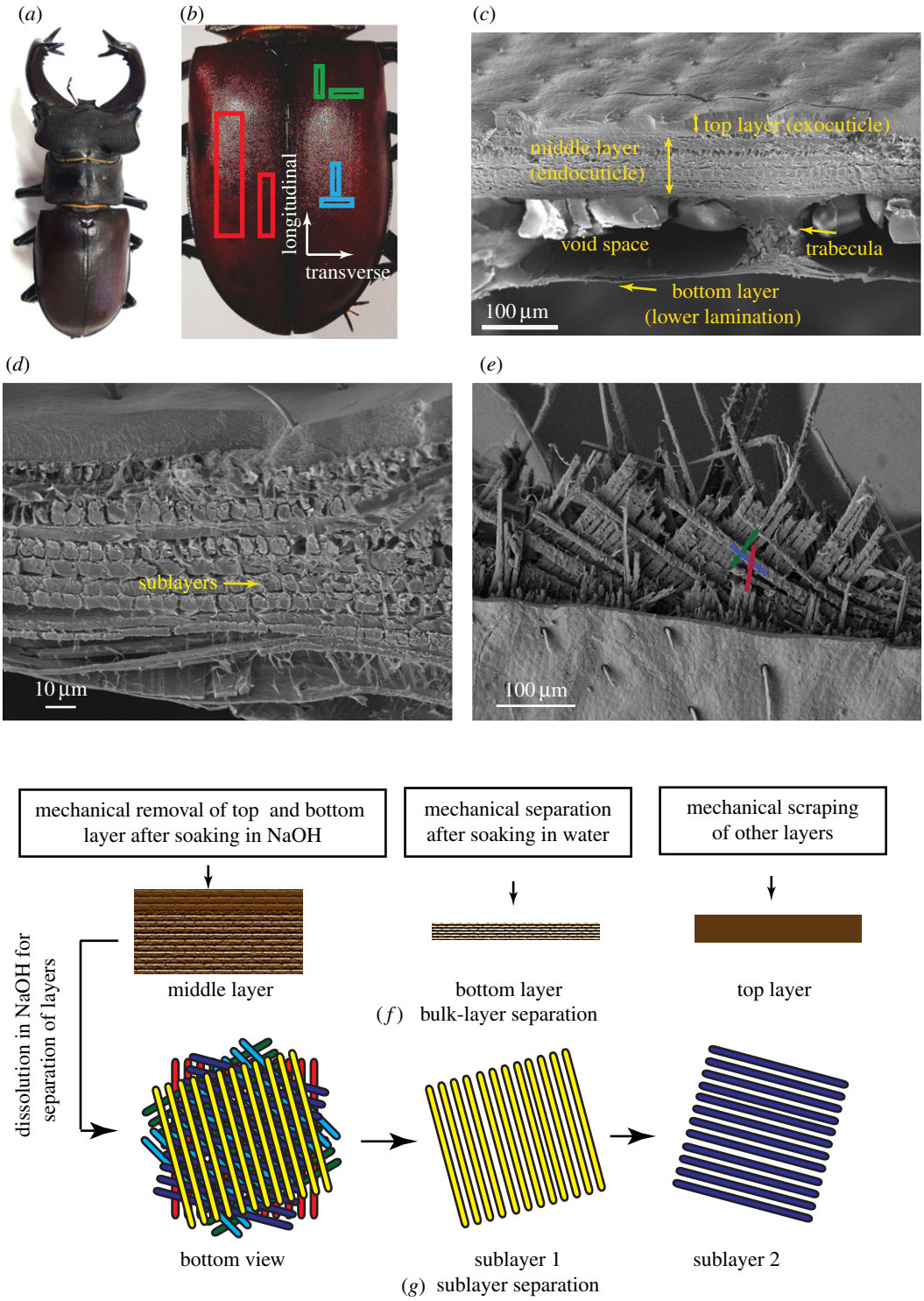

Figure 1. Sample preparation for mechanical testing: (*a*) image of the stag beetle species used in the study, (*b*) details of representative size and location of extracted samples (red = tension samples, green = samples used for in-plane anisotropy, blue = samples used for testing asymmetry in the out of plane direction). (*c*) SEM image of whole elytron cross section showing the constitutive bulk layers, void space and trabecular structures. (*d*) SEM image of the elytron cross section showing the endocuticle constitutive sublayers. (*e*) SEM image of the fractured elytron showing the macro-fibril orientation in endocuticle. (*f*) Schematic of procedures used for separation of bulk layers and (*g*) final separation of sublayers from the middle layer.

endocuticle primarily consists of stacked sublayers (figure 1*d*) and the fibre orientation changes from layer to layer (figure 1*e*). Constitutive bulk layers were separated using various procedures (figure 1*f*). Top layer was separated by mechanically peeling the bottom layer and carefully scraping the middle layer using a scalpel blade. The bulk middle layer was isolated after soaking the elytron with bottom layer removed, in 10% NaOH solution for 4 h that enabled easy removal of the top layer. The bottom layer was carefully peeled off from the whole elytron after soaking in water overnight. All the layers were allowed to dry for 24 h before testing to minimize the hydration effects during the separation processes. Tensile tests (two samples each from four beetles) and bending tests (three samples each from four beetles) on bulk layers were performed on the sections cut from the middle region of elytra as shown in figure 1*b*. Sublayers of the middle layer were also separated one by one after soaking the elytra in 10% NaOH for 2 days, which was proved to dissolve the protein matrix to an extent making the separation easy (figure 1*g*).

For this study, 'natural' loading condition was defined as the scenario in which the elytra would be subjected to forces on the

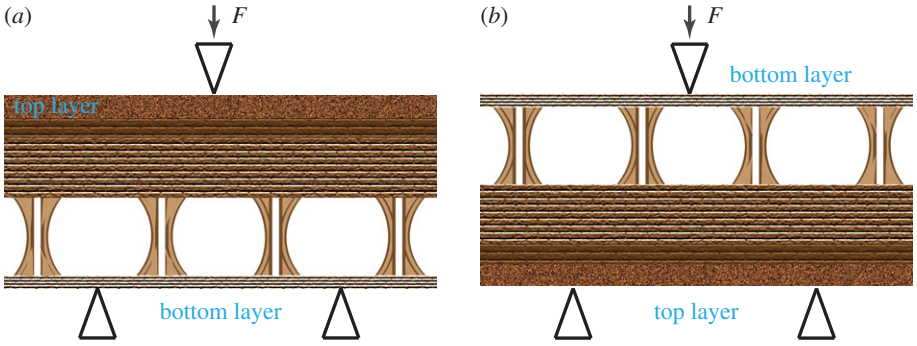

Figure 2. Schematic of three-point bending for testing (*a*) the natural loading condition and (*b*) the unnatural loading condition.

outermost epicuticular layer, either by the mandible of an opponent beetle during a fight or at the time of impact due to fall from a tree on the dorsal side (figure 2*a*). 'Unnatural' loading condition was defined as elytra being subjected to hypothetical loads from inside by the abdomen expansion, which is unlikely (figure 2*b*). The words 'natural' and 'unnatural' thus have been adopted to specify the loading direction. The flexural stress (σ) and strain (ε) from bending experiments were calculated using the following equations from the theory of beams, respectively:

$$\sigma = \frac{3Fl}{2wt^2} \tag{2.1a}$$

and

$$\varepsilon = \frac{6\delta t}{l^2}, \tag{2.1b}$$

where F is the applied bending force and δ is deflection at the midspan (from the measurements), w is the beam width, l is the span and t is the thickness. The above calculations were made assuming that the multilayer is homogeneous and thus that the maximum stress values occur at the bottom and top chords of the cross section.

2.3. Analytical modelling

The global tensile properties, i.e. stiffness and strength, of the multilayer system obtained from experiments were verified by a simple rule of mixtures taking into account the contribution of each layer, assuming perfect bonding between them:

$$E_{\text{elytra}} = \sum_{i=1}^{n} f_i E_i \tag{2.2a}$$

and

$$\sigma_{\text{elytra}} = \sum_{i=1}^{n} f_i \sigma_i, \tag{2.2b}$$

where f_i is the volume fraction of each layer, that is, the ratio of their thickness over the overall thickness of the elytron. The derivation of bending properties for a multilayer beam is described in the following [22]. Assuming all material laws as linear elastic and isotropic, a homogenization factor $E_i(y)/E_r$, defined as the ratio of elastic modulus of each material layer to an arbitrary reference modulus E_r, is used to determine the homogenized cross-section geometrical properties. The stress distribution along the thickness coordinate y of a beam subjected to axial load N and bending moment M can be evaluated according to the classical Navier's formula, under the hypothesis of planar deformation of bent sections

$$\sigma = \frac{E_i(y)}{E_r}\left(\frac{N}{A^*} + \frac{M}{I^*}(y - \bar{y})\right), \tag{2.3}$$

where $(y - \bar{y})$ is the coordinate with respect to the level of elastic centroid $\bar{y}$, A^* is the homogenized cross-section area defined as

$$A^* = \int_A \frac{E(y)}{E_r}\,\mathrm{d}A \tag{2.4}$$

and I^* is the homogenized beam moment of inertia with respect to the beam elastic centroid $\bar{y}$:

$$I^* = \int_A \frac{E_i(y)}{E_r}(y - \bar{y})^2\,\mathrm{d}A = \int_{y_i}^{y_e} \frac{E_i(y)}{E_r}(y - \bar{y})^2 w\,\mathrm{d}y, \tag{2.5}$$

where w is the beam section width, y_i, y_e are the coordinates of the bottom and top chords of the beam, respectively, with respect to the position of the elastic centroid $\bar{y}$ which can be calculated by the following expression:

$$\bar{y} = \frac{\sum_{i=1}^{n} E_i/E_r w t_i y_{G,i}}{\sum_{i=1}^{n} E_i/E_r w t_i}, \tag{2.6}$$

where E_i, t_i are the Young's moduli and thicknesses of each layer, respectively, and $y_{G,i}$ is the coordinate of the centroid of each layer with respect to an arbitrary reference origin. Equation (2.6) is obtained by posing the beam homogenized static moment equal to zero:

$$S^* = \int_A \frac{E_i(y)}{E_r}(y - \bar{y})\,\mathrm{d}A = 0. \tag{2.7}$$

Accordingly, the flexural modulus of the whole elytra can be calculated as

$$E_f = 12\frac{E_r I^*}{wt^3}, \tag{2.8}$$

where t is the total height of the beam. Finally, in accordance with the three-point bending scheme, the maximum transversal force at failure is

$$F_{\max} = \frac{4}{l}\frac{\sigma_f(y) I^*}{y_{i,e}}, \tag{2.9}$$

which is obtained by imposing that the maximum bending moment that the beam is able to carry under the three-point bending scheme ($M_{\max} = F_{\max} l/4$, at the midspan section) is reached when the current flexural stress (equation (2.1*a*)) reaches the failure strength of the corresponding materials σ_f at the bottom or top chords of the beam (y_i and y_e coordinates, respectively).

2.4. Computation modelling

A FEM model was developed to simulate three-point bending tests and elucidate the deformation/failure mechanism in the elytra. The multilayer was modelled assuming that the constitutive materials of the layers follow a linear elastic and isotropic law, having the same behaviour in tension and in compression, as assumed in the analytical model. The average tensile

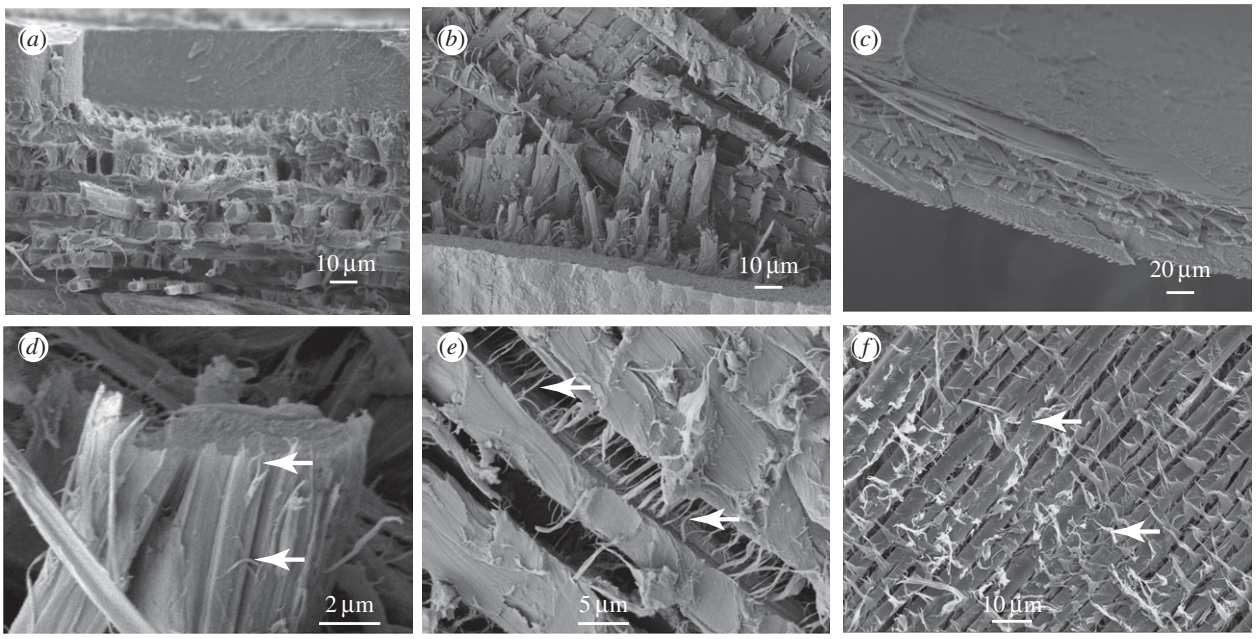

Figure 3. SEM images showing the microstructure of elytra. (*a*) Fractured cross section showing the exocuticle with relatively smooth surface and the endocutilce with change in fibre diameter and layer thickness from top to bottom sublayers. (*b*) Top view of fractured surface of elytron shows fibre rotation in sublayers. (*c*) Lower lamination made by a composite layer with sublayers made of relatively smaller fibre cross section. (*d*) Fractured fibre bundle showing its constitutive nano-fibres (arrows). (*e*) Interconnections (arrows) between fibre bundles in a layer. (*f*) A single separated sublayer shows the broken fibrillar connections (arrows) between two adjacent sublayers.

mechanical and geometrical properties of each layer determined from the experimental tests, i.e. elastic modulus, failure strength and strain, and thickness were used as input for simulations. Two cylindrical rigid bars are used to support the elytron beam and a third one at the midspan moves from the top under displacement control (same rate as experiments) in order to apply deflection. The simulated sample has the same dimension of the experiments. Details of the geometry can be found in electronic supplementary material, figures S2–S3. The top layer and trabecular structures were modelled with under-integrated solid elements with hourglass (spurious deformation modes) controlled. Middle and bottom layers are modelled with strain reduced integrated thick shell elements. These elements are specifically suitable for low thickness layers because they have the same degrees of freedom as a shell element but a physical thickness in place of a mathematical one. This allows a better treatment of contact, especially when the plies are subjected to out of plane compression, such as in our experiments. The details of the contact model are explained in the electronic supplementary material (finite element modelling details S1).

The FEM model to study the cushioning effect replaces the two rigid supports with a continuous elastic substrate, composed of two layers simulating the wing and the body of the animal. The mechanical properties of the body were assumed to be the same as that of the top layer of the elytra, because the abdominal external cuticle has similar multilayer structure. The single layer of wing has thickness of 4.4 µm and an elastic modulus $E = 3$ GPa [23]. The load application follows the same procedure described for the three-point bending set-up.

3. Results and discussion

3.1. Microstructure of elytra

Microstructural examination showed that elytra are multi-layered composites primarily comprising three bulk layers of different thickness. The exocuticle is just below the epicuticle that is exposed to the environment and the middle bulk layer comprised sublayers including microfibres (figure 3*a*). The tanned exocuticle consists of chitin microfibrils embedded helicoidally in a sclerotized protein matrix [24]. Fibre cross-section shape changes from nearly circular to square section from top to the bottom, along with reduction in the layer thickness (figure 3*a*). The fibre orientation in endocuticle gradually changes from the top to the bottom sublayer (figure 3*b*). This is similar to observation made in Japanese rhinoceros beetles, *Allomyrina dichotoma* [25]. The ventral layer referred to as bottom layer also has similar structure to that of endocuticle but with thinner sublayers (figure 3*c*). These fibres are bundles made up of thin chitin nano-fibres cross-linked with protein matrix (figure 3*d*). Thickness of each bulk layer was quantified for use in our theoretical and numerical modelling. The top layer has a thickness of 45 ± 4 µm and major contribution to the elytron thickness comes from the middle layer, with a thickness of 67 ± 5 µm. Elytron cross section obtained by fracturing showed a change in orientation of fibres between each layer (figure 3*b*). Such microstructural organization with changing fibre orientation in consecutive sublayers is referred to as the Bouligand structure and has been observed in elytra of other beetles [9], crab exoskeletons [26] and also in scales of fish dermal armours [27]. The change in angle of fibre alignment between consecutive sublayers in the middle layer is of about 78°. The bottom layer is the thinnest of all layers with a thickness of 8 ± 4 µm (figure 3*c*). We also observed interconnections between fibre bundles in a single sublayer that are crucial for inter fibre bundle bonding (figure 3*e*). These interconnections also enhance the interlaminar shear strength [28]. The microstructure of a single separated sublayer showed the out of plane interconnections that might play an important role in the overall mechanical response (figure 3*f*). Trabecular structures are pillar-like connections between the bottom and middle layers that are placed in rows along with pore canals (figure 4*a*). These trabecular

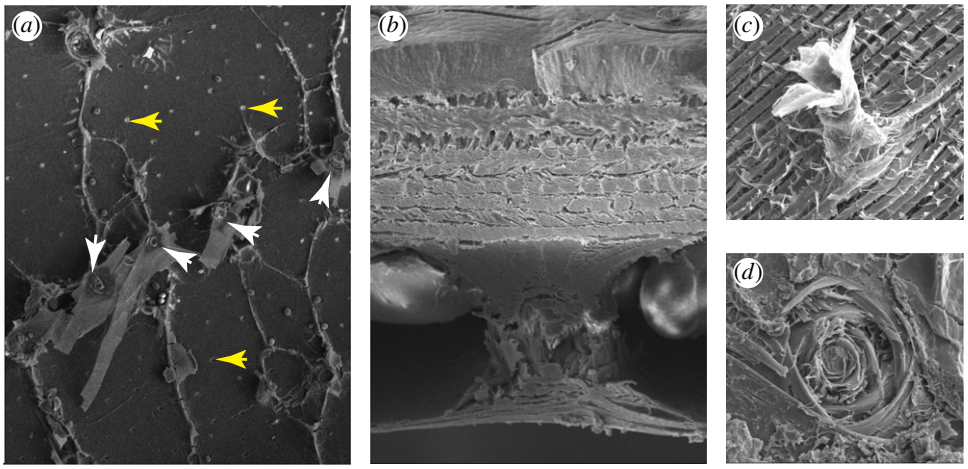

Figure 4. Elytra microstructure. (*a*) Large scanned area showing distribution pattern of trabecular structures of elytron (white arrows) and pore canals (yellow arrows). (*b*) Cross section showing how trabecular structure connects the middle and bottom layers. (*c*) Trabecular structure showing inner substructure after peeling of three layers as described in §2. (*d*) Top cross-sectional view of a trabecular structure showing concentric layers and their spiral woven structure.

structures have tapered cylindrical shape with higher diameter at the bottom and the top, when compared to the middle (figure 4*b*). The empty space between the bottom and the middle layers is the void space created by the loss of haemolymph after resorption [29]. After mechanically removing three sublayers from the middle layer, trabecular structure shows a reduced diameter (figure 4*c*) and its fractured structure show the spiral winding of the layers around the core (figure 4*d*). The observed interconnections (figure 3*f*) are similar to the ribbon-shaped pore canal tubules in crab exoskeletons that were hypothesized to function as a ductile component connecting the fibre bundles to improve the toughness in the thickness direction [26]. In the mineralized shell of windowpane oyster (*Placuna placenta*), a different type of screw dislocation-like connection centre was observed to enhance the interface toughness by reducing the delamination [30].

3.2. Mechanical testing and modelling

3.2.1. Tensile strength and Young's modulus of the elytra

Stress–strain curves from these experiments showed repeatability in terms of a sudden drop in load that is representative of a brittle-like fracture of the cuticle (figure 5*a*,*b*). In large samples, the average values of fracture strength and modulus of elytra were 65.0 ± 25.5 MPa and 1.9 ± 0.6 GPa, as reported in table 1. In the case of small size samples, the average values of fracture strength and modulus of elytra were 81.7 ± 35.1 MPa and 1.29 ± 0.5 GPa, as shown in table 1. This sample-size-dependent variation can be attributed to the presence of trabecular structures and pore canals acting as defects. So, the density and distribution of these structures could be a significant factor. If we consider the surface area of the samples, the larger samples have an average surface area of 17.3 mm^2 and the smaller samples have an average surface area of 1.75 mm^2. We investigated the scaling effects in tensile strength of the specimens. According to Weibull's (weakest link) theory, we expect:

$$\frac{\sigma_1}{\sigma_2} = \left(\frac{V_2}{V_1}\right)^{1/m}, \tag{3.1}$$

where σ and V are the tensile strength and volume of the specimens, respectively. The estimated value of the Weibull modulus m is 10.25. Similarly, according to an energy dissipation on a fractal volume of dimension D [31], we expected

$$\frac{\sigma_1}{\sigma_2} = \left(\frac{V_1}{V_2}\right)^{(D-3)/6}. \tag{3.2}$$

The estimated value of D is 2.41 confirming a fractal domain intermediate between an Euclidean surface ($D = 2$) and volume ($D = 3$). Our whole elytron experimental results were comparable to those of other beetle species [17], in particular, Hercules beetle (*Dynastes hercules*) with elastic modulus and strength values in the range of 3.1–14 GPa and 26.8–62.9 GPa, respectively [32]. The large variability observed in fracture strength could be attributed to the biological variation, density and distribution of observable defects such as pore canals and trabecular structures, and in addition the effects introduced from the sample preparation. During preparation, it is difficult to create samples which are identical in terms of distribution and density of trabecular structures and of pore canals. In addition, the location of these structures has a significant effect depending on whether the cut was made through them or close to them. In such cases, these defects could possibly act as cracks and notches, if they are located on the edges of the sample (along the length) and close to the stress concentration regions, resulting in a significant reduction of fracture strength. By contrast, if these structures are not located at the edges, the sample could result in higher fracture strength. Such variations were also observed in the tanned elytra of *Tribolium castaneum* [33]. To understand the detailed contribution of various bulk layers, we have performed tensile tests on separated layers. The top layer has a nearly linear stress–strain response and failed suddenly with the load dropping to zero (figure 5*c*). Middle layer also displayed a linear stress–strain response but towards the end showed a slight drop in load corresponding to initiation of fibre delamination followed by a sudden failure (figure 5*d*). Bottom layer also displayed a linear stress–strain response and load dropped to zero with sudden failure (figure 5*e*). The top layer has a Young's modulus of 4.14 ± 0.46 GPa and a fracture strength of 203.5 ± 62.2 MPa. Whereas, the middle layer has a modulus of 2.73 ± 0.77 GPa and fracture strength of 124.5 ± 37.4 MPa. The bottom layer has a modulus of

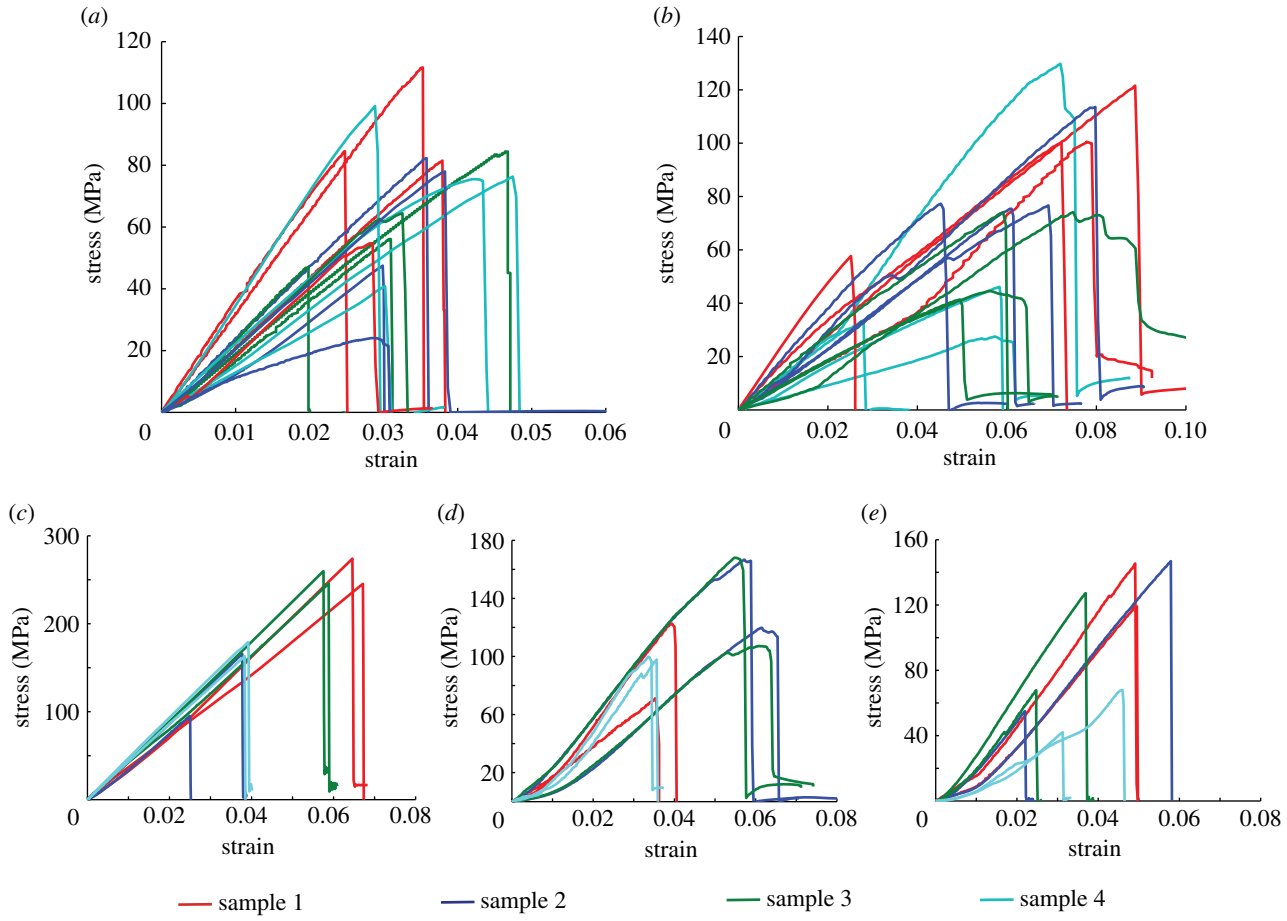

Figure 5. Stress–strain relationships showing mechanical behaviour from tension experiments of elytra: (*a*) larger samples showing brittle like fracture and (*b*) smaller size samples showing similar behaviour. (*c*) Top layer having a linear response with sudden failure, (*d*) middle layer also showing linear response with a drop due to initiation of fibre delamination followed by sudden failure, and (*e*) bottom layer also showing linear response with a sudden failure.

Table 1. Tensile mechanical properties of elytron and of its constitutive layers (in brackets: standard mean of error).

tensile mechanical properties		
cuticle/layer	Young's modulus (GPa)	fracture strength (MPa)
elytron (large)	1.90 ± 0.6 (0.23)	65.0 ± 25.5 (10.1)
elytron (small)	1.29 ± 0.5 (0.32)	81.7 ± 35.1 (21.4)
top layer	4.14 ± 0.46 (0.33)	203.5 ± 62.2 (63.1)
middle layer	2.73 ± 0.77 (0.19)	124.5 ± 37.4 (25.2)
bottom layer	2.62 ± 0.92 (0.93)	101.6 ± 46.6 (36.5)

2.62 ± 0.92 GPa and fracture strength of 101.6 ± 46.6 MPa. Thus, top layer has stiffer response and also higher failure strength, as compared to other bulk layers. Using the measured mechanical properties of single layers, by a classical rule of mixture (equations (2.2*a*,*b*), see Materials and methods section), we estimated Young's modulus and tensile strength of multilayer to be 2.1 GPa and 85.8 MPa, respectively. These estimates are comparable with the experimentally measured values of the whole elytron.

It emerges that tensile strength gradually decreases from top layer to bottom layer and stiffness also followed a similar trend which could be an optimization for puncturing resistance. In tension, failure was observed as a brittle fracture propagating in the top hard layer, pull-out and breaking of fibres in the other layers. The observed bridging fibres between adjacent fibre bundles and also between sublayers aid in increasing the fracture resistance (figure 3*e*,*f*). Overall, the Bouligand (helicoidal) structure of the layers is known to increase the fracture toughness [34,35].

3.2.2. Flexural modulus and flexural strength of elytra

Experimental flexural stress–strain curves showed a nearly linear response up to failure and the dispersion in the mechanical properties is significant (figure 6*a*,*b*). Flexural strength and flexural modulus were 312 ± 103 MPa and 451 ± 91 MPa, respectively, in the longitudinal direction. A similar range of values of flexural strength (333 ± 94 MPa) and flexural modulus (421 ± 59 MPa) was observed in the orthogonal transverse direction. These results demonstrate that there is no significant anisotropy in the bending response of elytra at a given location. To examine the dependency of loading condition on bending behaviour of elytra, we performed a second set of bending experiments. Stress–strain curves from these experiments were observed to be significantly different (figure 6*c*,*d*). In natural loading condition, some specimens failed suddenly and some failed gradually with progressive damage. In the case of unnatural loading condition, step-wise load drop was observed with increasing strain after a certain deflection. Flexural strength and flexural

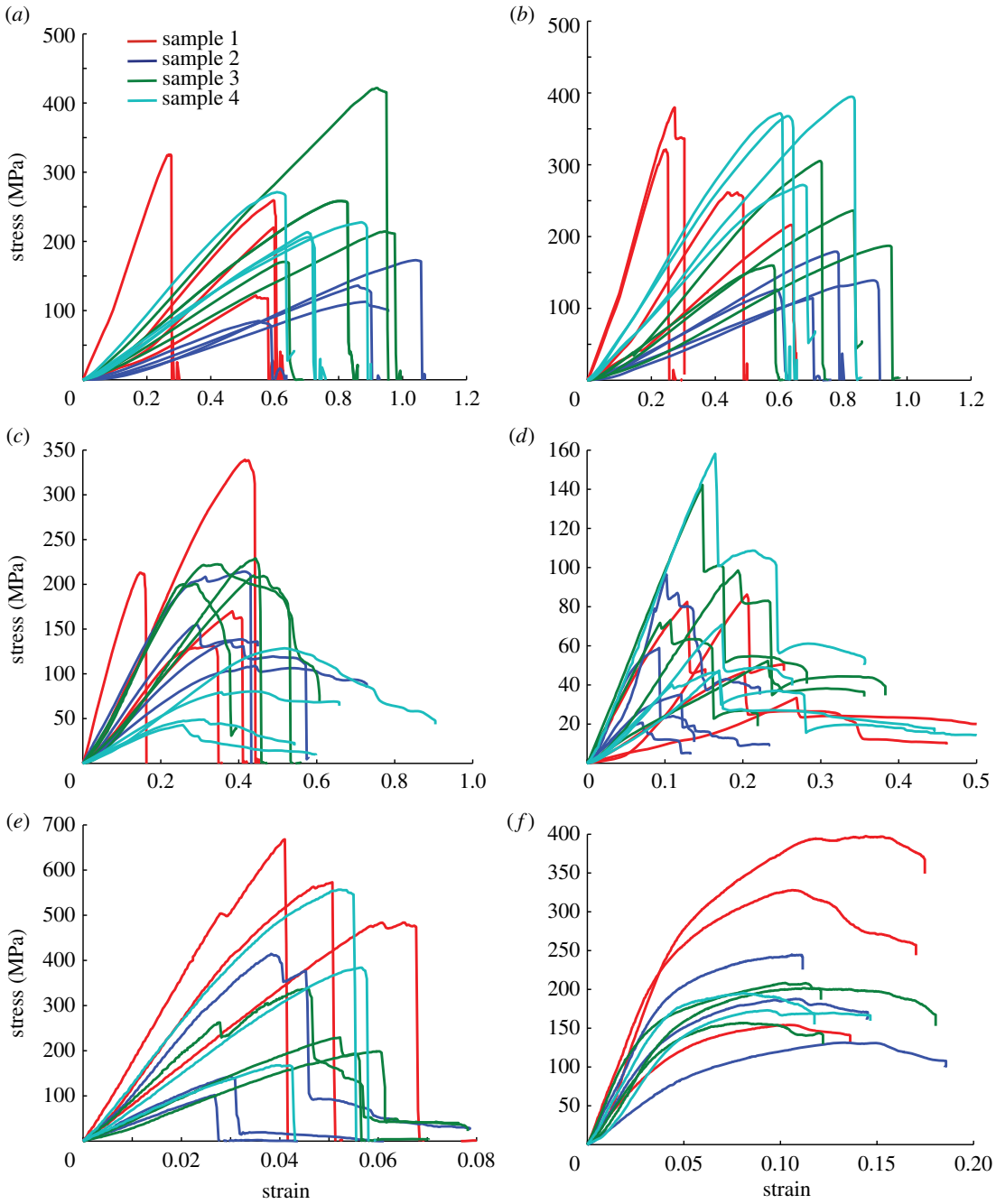

Figure 6. Bending stress–strain curves from elytra along (*a*) longitudinal direction and (*b*) transversal direction. Second set of experiments on elytra under (*c*) natural loading condition and (*d*) unnatural loading condition. Natural bending in longitudinal direction of (*e*) top layer and (*f*) middle layer.

Table 2. Flexural mechanical properties of elytron and of its constitutive layers (in brackets: standard mean of error).

bending mechanical properties		
layer	flexural strength (MPa)	flexural modulus (MPa)
elytron natural direction	222 ± 172 (138)	811 ± 650 (420)
elytron unnatural direction	73 ± 39 (17)	455 ± 287 (135)
top layer	392 ± 178 (99)	8295 ± 4745 (1543)
middle layer	221 ± 85 (52)	3952 ± 1452 (612)

modulus in natural loading direction were 222 ± 172 MPa and 811 ± 650 MPa, respectively. In unnatural loading direction, the values of flexural strength and flexural modulus were 73 ± 39 MPa and 455 ± 287 MPa, respectively, i.e. nearly one-half with respect to the real operating scenario (table 2). Such high variability in modulus and strength for each configuration can be attributed to the inherent biological differences in our extracted beetle samples, regional variation in the elytra and the limited availability because of their endangered status. The variation in properties from hinge location to mid location was in agreement with earlier observations made on five species of beetles [36]. Flexural modulus values are lower than that of tensile modulus, and this is also affected by the void space in elytra. By contrast, flexural strength is nearly three times that of the tensile strength. This

Table 3. Summary and comparison of experimental, analytical and simulation results of elytra mechanical properties.

		experiments	analytical	FEM simulations
tensile properties	σ (MPa)	81.7 $\pm$ 35.1	85.8	—
	E (GPa)	1.29 $\pm$ 0.50	2.10	—
bending properties	$E_{f,n}$ (GPa)	0.81 $\pm$ 0.65	1.46	0.94
	$E_{f,u}$ (GPa)	0.46 $\pm$ 0.28	0.96	0.83
	$\sigma_{f,n}$ (GPa)	0.22 $\pm$ 0.14	0.14	0.26
	$\sigma_{f,u}$ (GPa)	0.07 $\pm$ 0.04	0.07	0.09
	$F_{max,n}$ (N mm^{-1})	2.98 $\pm$ 1.82	2.31	3.31
	$F_{max,u}$ (N mm^{-1})	1.20 $\pm$ 0.64	1.15	1.15

is a noteworthy observation in elytra mechanics, with a higher mechanical strength in bending with respect to tension, due to the smaller high-stress regions in bending. Such observations were also made in glass fibre-reinforced polyamide composite materials [37]. The observed higher bending performance in elytra natural loading condition is similar to the behaviour of functionally graded ceramic engineering materials [38], where the asymmetric bending behaviour is achieved by varying the composition of the ceramic components.

Stress–strain curves of top layer displayed behaviour similar to that of a brittle material and that of the middle layer were similar to a ductile material (figure 6*e*,*f*). Results from these tests showed that the top layer has a flexural strength of 392 $\pm$ 178 MPa and flexural modulus of 8.29 $\pm$ 4.74 GPa, while the flexural strength and flexural modulus of middle layer were measured to be 221 $\pm$ 85 MPa and 3.95 $\pm$ 1.45 GPa, respectively (table 2). The exocuticle of elytra of giant water bugs (*Hydrocyrius columbiae*) was observed to have microfibrils of diameter approximately 45 Å and centre to centre distance of approximately 65 Å, and to be arranged helicoidally with a rotation of 6–7° per plane [39]. These densely packed chitin microfibrils embedded in tanned protein matrix might act as reinforcements and the helicoidal arrangement results in isotropic and enhanced stiffness of the exocuticle. Such improvement in mechanical properties due to the presence of the helicoidal fibre arrangement has been proved by testing bioinspired laminate composites [40]. Flexural modulus of these layers was an order of magnitude higher and flexural strength was of the same order, as compared to the whole elytron. It was not possible to measure flexural properties of the bottom layer using the current experimental set-up, because of its extremely low thickness and bending stiffness, thus negligible here.

The position $\bar{y}$ of the neutral axis, that is the level at which the bending stresses and strains change sign, is calculated to be approximately 12 µm below the interface between the top and the middle layers, using average values of each layer's elastic modulus and thickness. To analyse the role of trabecular structures, in particular of their height, we analysed the role of the void space between middle and bottom layers by varying it in the analytical calculations from 0 to 80 µm. According to equation (2.3), we obtained that the distance of neutral axis would be in the range of 9 to 13 µm, thus the relative position of the elastic centroid is nearly constant within the endocuticle, suggesting another role for the void space other than optimizing bending properties. On the other hand, the position of neutral axis is significantly affected by the variation in elastic modulus and thickness of each layer, as expected for a composite multilayer. This indicates that the multilayer grading sequence of thickness and elastic moduli is optimized for better mechanical performance in bending. In particular, the elytron multilayer combination is a suitable design for the natural loading conditions, because the position of the elastic centroid confines compression stresses in the top brittle layer and tension in the tough composite middle layer, optimizing the local stress state for the specific constitutive laws of materials. This results in a ratio of about 3 between the bending mechanical properties in the two opposite directions (table 3).

The FEM simulations resembling three-point bending tests (figures 7 and 8) were performed to closely understand the mechanics of bending deformation and fracture behaviour. Results were consistent with experiments predicting the variation in flexural modulus and flexural strength in different loading conditions, despite the approximation of linear elastic isotropic material and same constitutive behaviour in tension and compression for each layer. In natural loading condition, an initial load drop (figure 7, point 2) was observed due to delamination in the middle layer and failure of the bottom layer, which suggests an optimized design of the bottom layer and interlamellar strength. The latter, assumed as a free parameter, allowed us to obtain the closest response with respect to the average force displacement bending curve of elytra (see electronic supplementary material, figure S4). The results suggest optimal interface shear strength ($\tau_{lim} = 5.5$ MPa) in the elytron multilayers. Similar findings were observed in impact simulations based on composite armours [41]. The final drop occurs when the whole elytron fails (figure 7*a*). After the first drop (point 2), a recovery of the load with reduced stiffness at point 3 is attributed to the bending resistance from the intact top layer and middle layer. The deformation sequence is shown using snapshots of simulation corresponding to various stages of deformation and complete failure (figure 7*b*). In the unnatural loading condition, buckling of bottom layer was observed as it experiences compression and its contribution to flexural modulus and strength becomes nearly negligible (figure 8*a*), causing the first drop in the force (point 2). Delamination within the middle layer results in second load drop (figure 8*b*, point 3) and a consequent further flexural stiffness reduction. Complete fracture of the whole elytron starts from the failure of the hard layer at

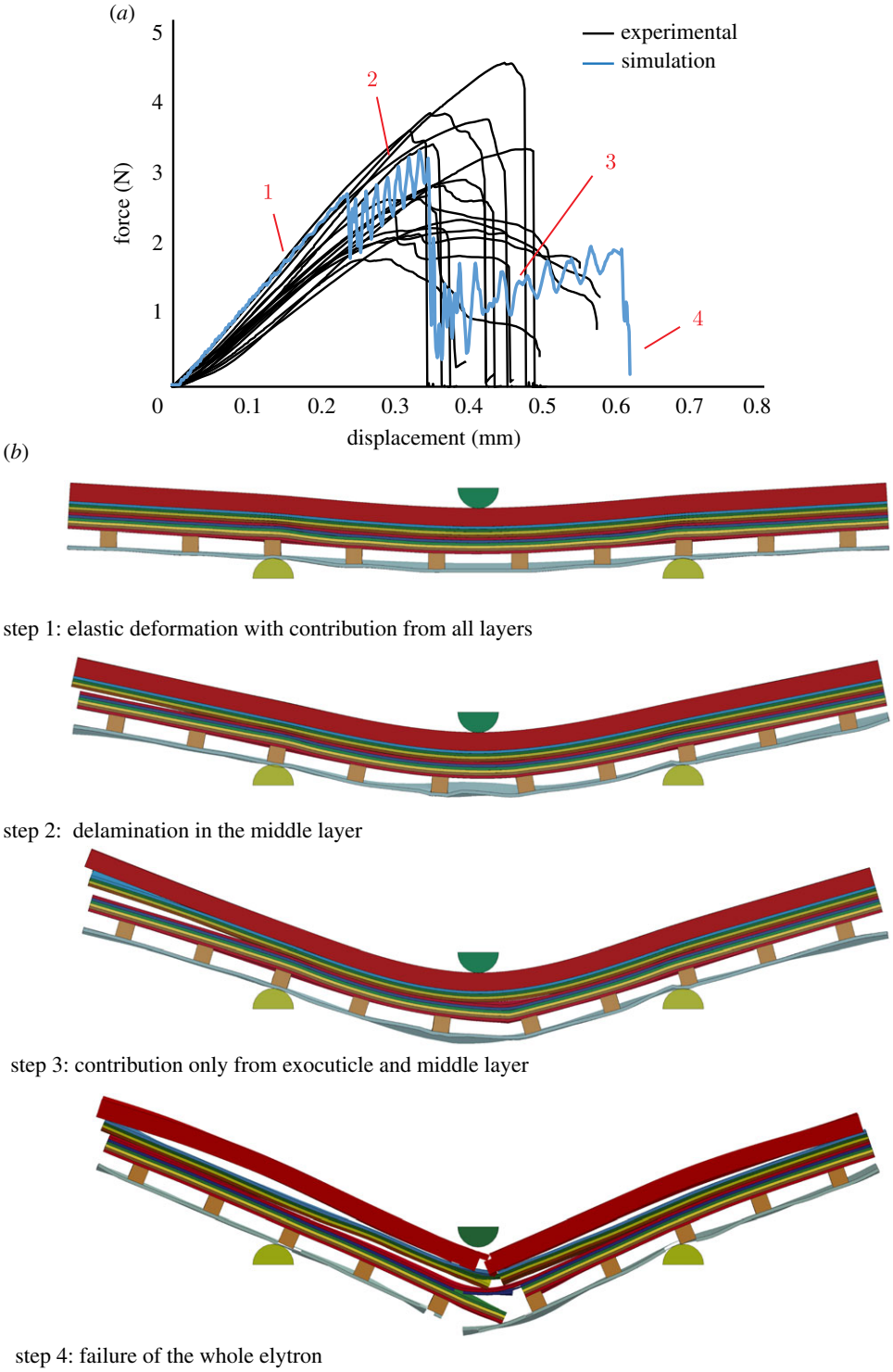

Figure 7. FEM simulation results of bending in natural loading condition showing (*a*) the force displacement relationship and (*b*) snapshots of the corresponding stages of bending.

the bottom in this configuration (point 4). Thus, failure in this condition initiates from top layer depending on its tensile properties, followed by delamination in the middle layer and final overall collapse. Thus, we claim that the bottom layer is able to play a crucial role only in natural loading bending response. Simulations are in good quantitative agreement with experimental results.

It should be noted that all the experiments were performed on dehydrated specimens because of the near threatened (IUCN Red List) state of the selected species. As described in earlier studies, dehydration may significantly increase the mechanical properties of the cuticle [40]. So the mechanical properties of the whole elytron specimens must be considered in our study as related to the dried samples and as upper bound of living samples. Also an artificial rehydration cannot be considered representative of the living material, for which in any case the non-symmetric bending properties are also expected as confirmed by the related nonlinear mechanism (buckling of the bottom layer). Moreover, the sublayer separation methods could have affected their mechanical properties, i.e. by damaging layers and thus reducing the properties as compared to the properties in the native state. However, the numerical and analytical comparisons (which use single layer properties as inputs) with the experimental measurements on

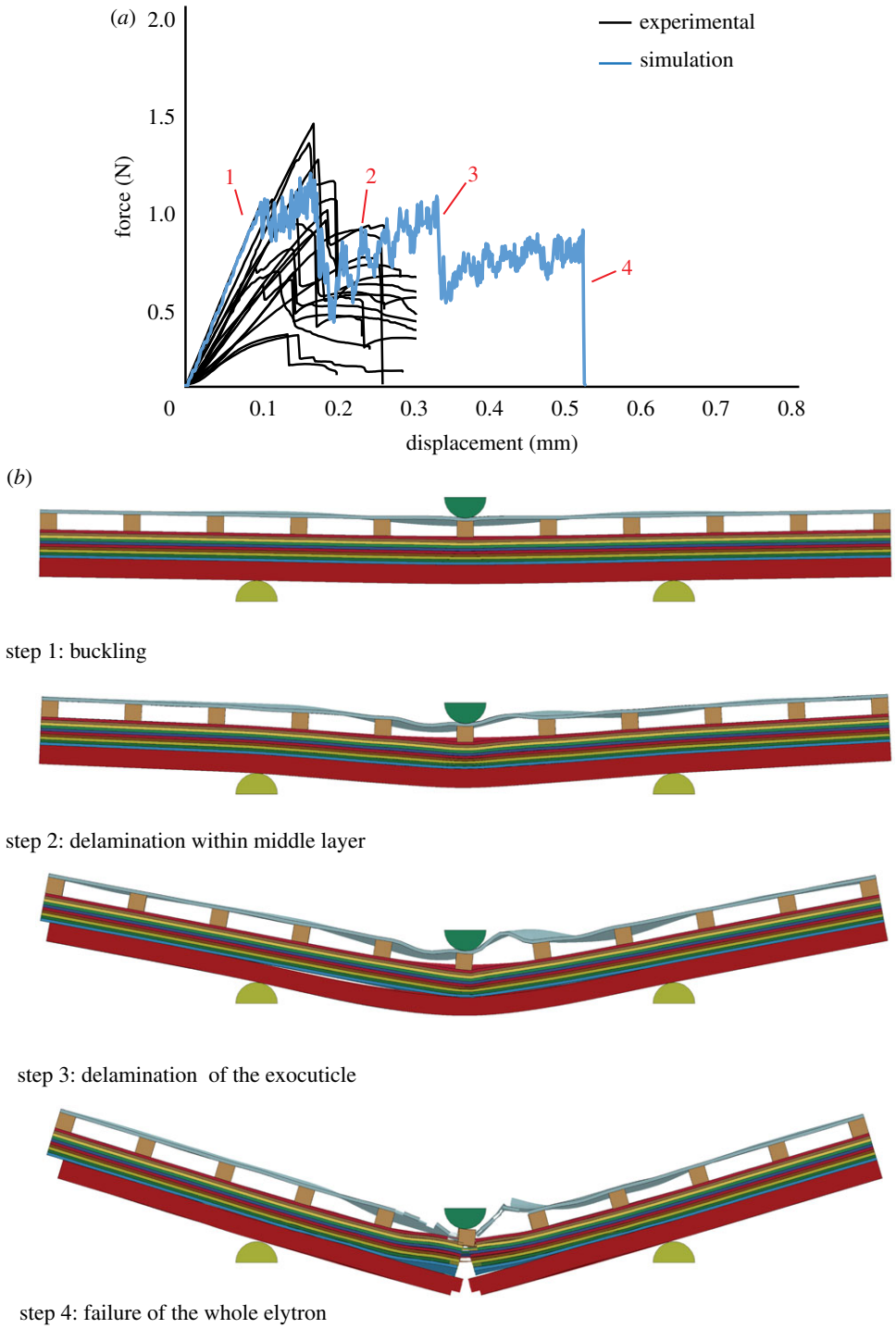

Figure 8. FEM simulation results of bending in unnatural loading condition showing (*a*) the force displacement relationship and (*b*) snapshots of the corresponding stages of bending.

the multilayered elytra suggest a limited alteration of properties during the layer separation process.

According to the experimental and simulation observations we can define two mechanisms in relation to the direction of bending. Under natural loading all the layers contribute to bending stiffness, whereas in the unnatural bending the contribution of the bottom layer can be neglected as it experiences buckling in compression due to its low thickness. Thus, in the natural loading case, the total thickness of the multilayer enters into play, while in the unnatural loading case, only the thickness of top and the middle layers could be considered. According to equation (2.8), we estimate the flexural moduli in the two loading conditions $E_{f,n} = 1.46$ GPa and $E_{f,u} = 0.96$ GPa, where the subscripts n and u denote the natural and unnatural loading conditions, respectively. From equation (2.9), in the case of natural bending, first failure occurs in the bottom layer, corresponding to a bending force $F_{max,n} = 2.98\ \mathrm{N\ mm^{-1}}$. After that, the reactive section is composed by just the top and middle layers and the overall failure of the multilayer occurs for the rupture in tension of the middle layer. In the unnatural bending case, the maximum force at failure is given by the rupture of top layer at $F_{max,u} = 1.15\ \mathrm{N\,mm^{-1}}$. Both analytical and simulation results are in good agreement with experiments. The final plateau region obtained both in FEM simulation and experiments corresponds to the friction slipping of the sample at the contact points (figure 8*b*). Results from experiments, simulation and analytical calculation are summarized for comparison in table 3.

In the real situation, the elytron and the folded wing underneath it are continuously supported by the body. The trabecular structures with the void space between them may provide a cushioning effect to further protect the fragile wing and the body from external loads. The supports of the three-point bending set-up are substituted by a continuous substrate simulating the insect wing and body under the protective elytra. In electronic supplementary material, figure S5, the distribution of stresses in the wing and the body under the same concentrated load ($F_{max,n}$, previously determined) is depicted. Simulation results showed that elytron structure is subjected to local higher stresses due to the presence of void space inside as compared to the case without it (3.9 MPa versus 2.9 MPa), because trabecular structures concentrate the load, but performed better in absorbing the energy. Indeed, under the same external load F, the total strain energy in the body was less than one-half compared to the elytron model without void space (2.2 µJ versus 4.92 µJ). This is a good indication that the presence of the void space in elytra helps in mitigating the energy transfer to the body by allowing higher deformation of the top layers and spreading the load over a larger area (electronic supplementary material, figure S5). In some beetles, the void space could be filled haemolymph but because we are not sure of its occurrence in the natural state of our study species, we have not considered this complex scenario.

4. Conclusion

Characterization of stag beetle elytra by means of mechanical experiments, theory and simulations gave a new insight into the role of microstructure in their mechanical behaviour. Particularly, the synergy between materials and structural arrangement by combination of layer stacking results in enhanced stiffness and load bearing capacity upon bending. The combination of hard top layer performing better in compression and the flexible bottom layer that contributes only in tension is optimized to provide higher bending stiffness in natural loading condition. Also, the position of flexible bottom layer far away from the centroid of the cross section with the aid of connecting trabecular structures allows the beetle to reduce the cuticle weight by maximizing the moment of inertia, and thus flexural strength and modulus. At the same time, this structure provides cushioning capability, reducing the energy transfer to the beetle body and internal organs. FEM simulations developed in this study have the capability of modelling fracture and large deformations and could be extended to other biological structures similar to elytra or to their engineering bioinspired designs. These results could help in designing structures such as body armours with asymmetric bending properties tuned to perform better in terms of energy absorption and strength in a particular loading condition, with improved ergonomics and flexibility together with external rigidity.

Data accessibility. This article has no additional data.

Authors' contributions. L.K. and N.M.P. designed the study. M.M. helped in acquiring the samples. H.S.G. contributed in technical discussions and manuscript editing. L.K. performed the mechanical experiments. S.S. performed the FEM simulations. L.K. and S.S. wrote the first draft of the manuscript (corresponding sections). N.M.P. supervised the study and developed the analytical model. All authors approved the contents of the article.

Competing interests. The authors declare no conflict of interest.

Funding. N.M.P. is supported by the European Commission H2020 under the Graphene Flagship Core 2 grant no. 785219 (WP14, Composites) and under the FET Proactive ('Neurofibres' no. 732344), as well as by the Italian Ministry of Education, University and Research (MIUR) under the 'Departments of Excellence' grant no. L.232/2016. N.M.P is also supported by Fondazione Caritro under 'Self-Cleaning Glasses' no. 2016.0278, as L.K. S.S. acknowledges financial support from Ermenegildo Zegna Founder's Scholarship 2017–2018.

Acknowledgement. The authors thank Nicola Angeli (MUSE, Trento) for the help with SEM imaging and Ludovic Taxis for his guidance and help with the initial experiments.

References

1. Vincent JFV, Wegst UGK. 2004 Design and mechanical properties of insect cuticle. *Arthropod. Struct. Dev.* **33**, 187–199. (doi:10.1016/j.asd.2004.05.006)
2. Gunderson S, Schiavone R. 1989 The insect exoskeleton: a natural structural composite. *J. Miner. Met. Mater. Soc.* **41**, 60–62. (doi:10.1007/BF03220386)
3. Vincent JFV. 2002 Arthropod cuticle: a natural composite shell system. *Compos. A Appl. Sci. Manuf.* **33**, 1311–1315. (doi:10.1016/S1359-835X(02)00167-7)
4. Hadley NF. 1986 The arthropod cuticle. *Sci. Am.* **255**, 104–112. (doi:10.1038/ scientificamerican 0786-104)
5. Hopkins TL, John Krchma L, Ahmad SA, Kramer KJ. 2000 Pupal cuticle proteins of manduca sexta: characterization and profiles during sclerotization. *Insect Biochem. Mol. Biol.* **30**, 19–27. (doi:10.1016/S0965-1748(99)00091-0)
6. Roux-Pertus C, Oliviero E, Viguier V, Fernandez F, Maillot F, Ferry O, Fleutot S, Mano JF, Cleymand F. 2017 Multiscale characterization of the hierarchical structure of *Dynastes hercules* elytra. *Micron* **101**, 16–24. (doi:10.1016/j.micron.2017.05.001)
7. Bar-On B, Barth FG, Fratzl P, Politi Y. 2014 Multiscale structural gradients enhance the biomechanical functionality of the spider fang. *Nat. Commun.* **5**, 3894. (doi:10.1038/ncomms4894)
8. Peisker H, Michels J, Gorb SN. 2013 Evidence for a material gradient in the adhesive tarsal setae of the ladybird beetle *Coccinella septempunctata*. *Nat. Commun.* **4**, 1661. (doi:10.1038/ncomms2576)
9. Van de Kamp T, Greven H. 2010 On the architecture of beetle elytra. *Entomol. Heute* **22**, 191–204.
10. Guo T, Wang Y-F. 2011 Energy absorbing structures imitating trabecular of beetle cuticles. *Eng. Mech.* **28**, 246–256.
11. Stavenga DG, Wilts BD, Leertouwer HL, Hariyama T. 2011 Polarized iridescence of the multilayered elytra of the Japanese jewel beetle, *Chrysochroa fulgidissima*. *Phil. Trans. R. Soc. B* **366**, 709–723. (doi:10.1098/rstb.2010.0197)
12. Onelli OD, Van de Kamp T, Skepper JN, Powell J, Rolo TDS, Baumbach T, Vignolini S. 2017 Development of structural colour in leaf beetles. *Sci. Rep.* **7**, 1373. (doi:10.1038/s41598-017-01496-8)
13. Le TQ, Van Truong T, Park SH, Truong TQ, Ko JH, Park HC, Byun D. 2013 Improvement of the aerodynamic performance by wing flexibility and elytra–hind wing interaction of a beetle during forward flight. *J. R. Soc. Interface* **10**, 20130312. (doi:10.1098/rsif.2013.0312)
14. Dai Z, Zhang Y, Liang X, Sun J. 2008 Coupling between elytra of some beetles: mechanism, forces and effect of surface texture. *Sci. China. C. Life Sci.* **51**, 894–901. (doi:10.1007/s11427-008-0124-7)
15. Chen J, Wu G. 2013 Beetle forewings: epitome of the optimal design for lightweight composite materials. *Carbohydr. Polym.* **91**, 659–665. (doi:10.1016/j.carbpol.2012.08.061)
16. van de Kamp T, Doerstelmann M, dos Sanots Rolo T, Baumbach T, Menges A, Knippers J. 2015 Beetle

elytra as role models for lightweight building construction. *Entomol. Heute* **27**, 149–158.

17. Goyens J, Dirckx J, Dierick M, Van Hoorebeke L, Aerts P. 2014 Biomechanical determinants of bite force dimorphism in *Cyclommatus metallifer* stag beetles. *J. Exp. Biol.* **217**, 1065–1071. (doi:10.1242/jeb.091744)
18. Lomakin J, Arakane Y, Kramer KJ, Beeman RW, Kanost MR, Gehrke SH. 2010 Mechanical properties of elytra from *Tribolium castaneum* wild-type and body color mutant strains. *J. Insect Physiol.* **56**, 1901–1906. (doi:10.1016/j.jinsphys.2010.08.012)
19. Sun J, Tong J, Zhang Z. 2009 Nanomechanical properties and the hierarchical structure of elytra cuticle of dung beetle (*Copris ochus* Motschulsky). In *Int. Conf. on Mechatronics and Automation*, *Changchun, China*, *9–12 August 2009*, pp. 4277–4282. (doi:10.1109/ICMA.2009.5246542)
20. Sun J, Tong J, Chen DH, Lin J, Liu X, Wang Y. 2010 Micro-tensile testing of the lightweight laminated structures of beetle elytra cuticle. *Adv. Nat. Sci.* **3**, 225–234. (doi:10.3968/g956)
21. Abràmoff MD, Magalhães PJ. 2004 Image processing with ImageJ. *Biophotonics Int.* **11**, 36–42.
22. Timoshenko S, Goodier J. 1970 *Theory of elasticity*. 3rd edn. New York, NY: McGraw Hill.
23. Ha NS, Jin TL, Goo NS, Park HC. 2011 Anisotropy and non-homogeneity of an *Allomyrina dichotoma* beetle hind wing membrane. *Bioinspir. Biomim.* **6**, 46003. (doi:10.1088/1748-3182/6/4/046003)
24. van de Kamp T, Riedel A, Greven H. 2016 Micromorphology of the elytral cuticle of beetles, with an emphasis on weevils (Coleoptera: Curculionoidea). *Arthropod Struct. Dev.* **45**, 14–22. (doi:10.1016/j.asd.2015.10.002)
25. Chen J, Dai G, Xu Y, Iwamoto M. 2007 Optimal composite structures in the forewings of beetles. *Compos. Struct.* **81**, 432–437. (doi:10.1016/j.compstruct.2006.09.006)
26. Chen P-Y, Lin AY-M, McKittrick J, Meyers MA. 2008 Structure and mechanical properties of crab exoskeletons. *Acta Biomater.* **4**, 587–596. (doi:10.1016/j.actbio.2007.12.010)
27. Zimmermann EA, Gludovatz B, Schaible E, Dave NKN, Yang W, Meyers MA, Ritchie RO. 2013 Mechanical adaptability of the Bouligand-type structure in natural dermal armour. *Nat. Commun.* **4**, 2634. (doi:10.1038/ncomms3634)
28. Ribbans B, Li Y, Tan T. 2016 A bioinspired study on the interlaminar shear resistance of helicoidal fiber structures. *J. Mech. Behav. Biomed. Mater.* **56**, 57–67. (doi:10.1016/j.jmbbm.2015.11.004)
29. Arakane Y, Lomakin J, Gehrke SH, Hiromasa Y, Tomich JM, Muthukrishnan S, Beeman RW, Kramer KJ, Kanost MR. 2012 Formation of rigid, non-flight forewings (elytra) of a beetle requires two major cuticular proteins. *PLoS Genet.* **8**, e1002682. (doi:10.1371/journal.pgen.1002682)
30. Li L, Ortiz C. 2015 A natural 3D interconnected laminated composite with enhanced damage resistance. *Adv. Funct. Mater.* **25**, 3463–3471. (doi:10.1002/adfm.201500380)
31. Carpinteri A, Pugno N. 2005 Are scaling laws on strength of solids related to mechanics or to geometry? *Nat. Mater.* **4**, 421–423. (doi:10.1038/nmat1408)
32. Conrad MB. 2014 Bioinspired composites design: mechanical and optical characterization of the Hercules beetle elytra. Master's thesis, Naval Post-Graduate School, California, USA.
33. Lomakin J, Huber PA, Eichler C, Arakane Y, Kramer KJ, Beeman RW, Kanost MR, Gehrke SH. 2011 Mechanical properties of the beetle elytron, a biological composite material. *Biomacromolecules* **12**, 321–335. (doi:10.1021/bm1009156)
34. Chen B, Peng X, Cai C, Niu H, Wu X. 2006 Helicoidal microstructure of Scarabaei cuticle and biomimetic research. *Mater. Sci. Eng. A* **423**, 237–242. (doi:10.1016/j.msea.2005.11.069)
35. Suksangpanya N, Yaraghi NA, Kisailus D, Zavattieri P. 2017 Twisting cracks in Bouligand structures. *J. Mech. Behav. Biomed. Mater.* **76**, 38–57. (doi:10.1016/j.jmbbm.2017.06.010)
36. Yu M, Hermann I, Dai Z, Gitis N. 2013 Mechanical and frictional properties of the elytra of five species of beetles. *J. Bionic Eng.* **10**, 77–83. (doi:10.1016/S1672-6529(13)60201-2)
37. Thomason JL. 2008 The influence of fibre length, diameter and concentration on the strength and strain to failure of glass fibre-reinforced polyamide 6,6. *Compos. A Appl. Sci. Manuf.* **39**, 1618–1624. (doi:10.1016/j.compositesa.2008.07.002)
38. Tsukada G, Sueyoshi H, Kamibayashi H, Tokuda M, Torii M. 2014 Bending strength of zirconia/porcelain functionally graded materials prepared using spark plasma sintering. *J. Dent.* **42**, 1569–1576. (doi:10.1016/j.jdent.2014.09.012)
39. Zelazny B, Neville AC. 1972 Quantitative studies on fibril orientation in beetle endocuticle. *J. Insect Physiol.* **18**, 2095–2121. (doi:10.1016/0022-1910(72)90243-0)
40. Cheng L, Thomas A, Glancey JL, Karlsson AM. 2011 Mechanical behavior of bio-inspired laminated composites. *Compos. A Appl. Sci. Manuf.* **42**, 211–220. (doi:10.1016/j.compositesa.2010.11.009)
41. Signetti S, Pugno NM. 2014 Evidence of optimal interfaces in bio-inspired ceramic-composite panels for superior ballistic protection. *J. Eur. Ceram. Soc.* **34**, 2823–2831. (doi:10.1016/j.jeurceramsoc.2013.12.039)
42. Klocke D, Schmitz H. 2011 Water as a major modulator of the mechanical properties of insect cuticle. *Acta Biomater.* **7**, 2935–2942. (doi:10.1016/j.actbio.2011.04.004)

Finite element modelling details

A cohesive-like separation law is implemented between the layers allowing failure of the interface and thus simulating the delamination. The interface will fail when the following condition is satisfied:

$$\left(\frac{\sigma}{\sigma_{lim}}\right)^2 + \left(\frac{\tau}{\tau_{lim}}\right)^2 \geq 1 \qquad \text{(S1)}$$

with σ_{lim} and τ_{lim} being the interface normal and shear limit strengths respectively. When failure occurs and the surfaces separate, the interaction automatically switches to a classical penalty based contact (static and dynamic coefficient of friction conventionally assumed 0.2. and 0.1). According to the Tresca criterion we have assumed $\tau_{lim} = \frac{1}{2}\sigma_{lim}$ and estimated the stresses, $\sigma_{lim} = 11$ MPa and $\tau_{lim} = 5.5$ MPa. This value was obtained by targeting the experiments bending modulus strength and strain given the material properties (Supplementary Figure S4). As the trabecular structures were observed to be formed by an extension of middle layer, the nodes surrounding trabecular top faces are welded together in order to simulate the degree of restrain between the two substructures (Supplementary Figure S3). Material failure is treated using erosion algorithm with failure that occurs when either one between the principal stress or strain reaches its limit, which corresponds to the average strength σ_f and strain $\varepsilon_f = \sigma_f/E$ measured from tensile tests (Supplementary Table S1). Failure of one element occurs when one integration point reaches the failure limit. Since the simulation is under control of the loading bar displacement, the external loading force F is measured indirectly from the normal contact force between loading bar and the layer in contact (that for equilibrium is equal to the one recorded at the two support bars).

Table S1. Characteristics and material properties of the layers used in the FEM model, taken as averages of the experimental results. ε_f is derived indirectly by σ_f/E assuming a linear elastic constitutive response for all layers.

Layer	Thickness [μm]	E [GPa]	σ_f [MPa]	ε_f
Epicuticle	45	3.23	93	0.029
Endocuticle	67	2.70	132	0.049
Void	39	-	-	-
Trabecular struct.	39	2.70	132	0.049
Lower lamination	8	2.29	156	0.068

Lakshminath Kundanati, Stefano Signetti, Himadri S. Gupta, Michele Menegon and Nicola M. Pugno (2018) Multilayer Stag Beetle elytra perform better under external loading via non-symmetric bending properties *J.Roc.Soc. Interface*

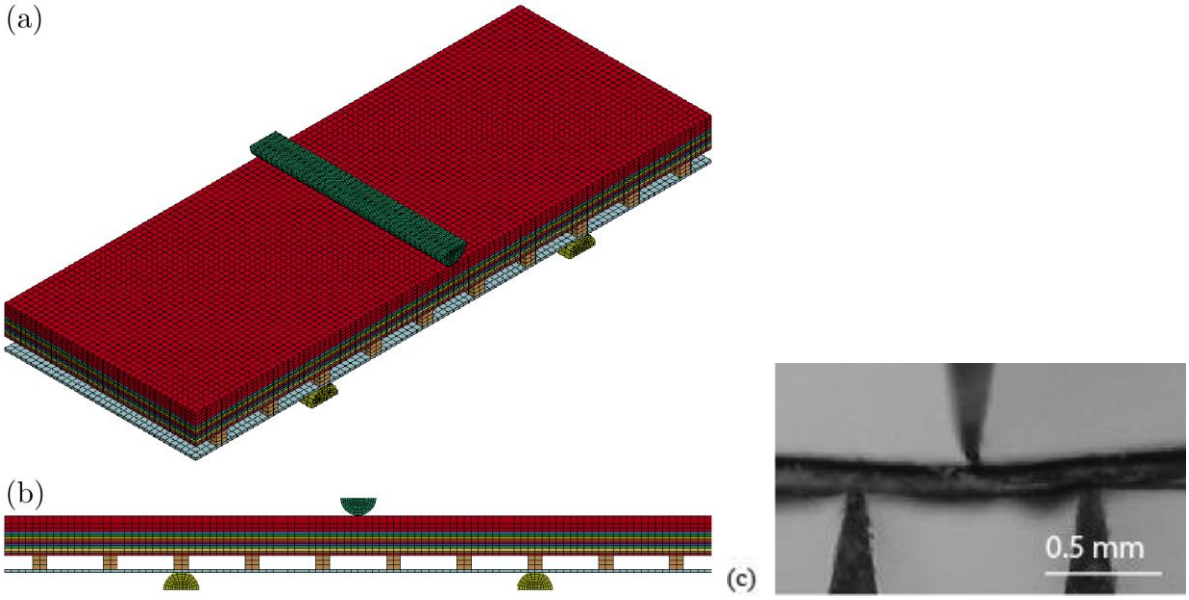

Figure S2. Images of the FEM model of the simulated three point bending test (a) isometric view, (b) lateral view (c) corresponding experimental sample set up.

Lakshminath Kundanati, Stefano Signetti, Himadri S. Gupta, Michele Menegon and Nicola M. Pugno (2018) Multilayer Stag Beetle elytra perform better under external loading via non-symmetric bending properties *J.Roc.Soc. Interface*

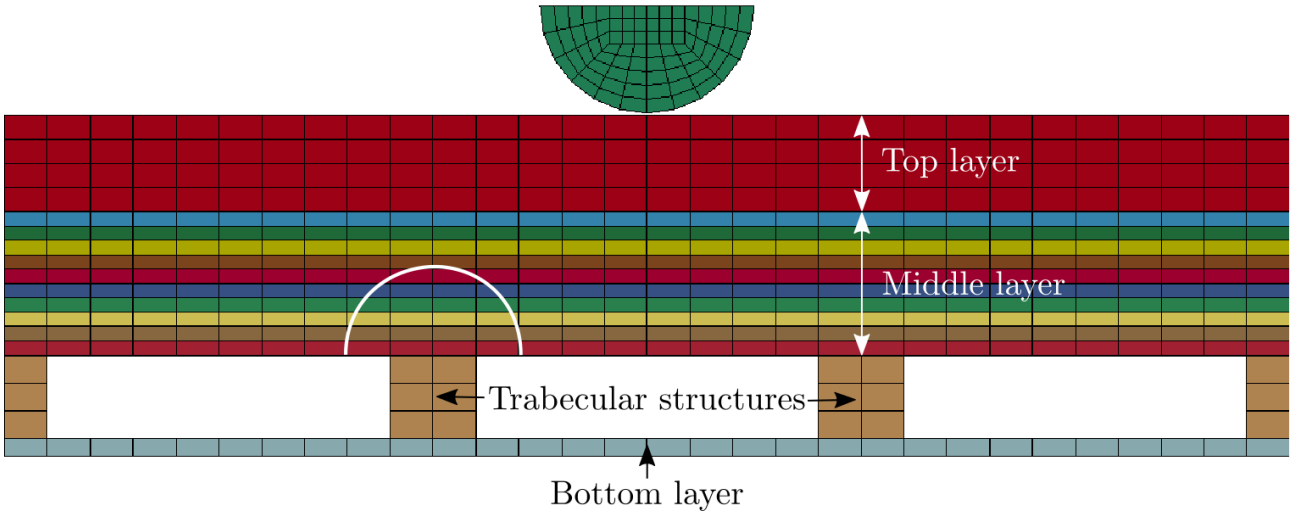

Figure S3. Detail of the FEM model with identification of the different elytra structures. The top layer and trabecular structures are built with solid elements while thick shell elements are used for the middle layer and the bottom layer. The encircled region corresponds to the volume of an hemisphere of radius *r* equal to the trabecular width for which the adjacent nodes of different layers are tied together, thus excluded from the delamination law. This solution was employed to taken into account the fact that trabecular structures are prolongations and folds of the layers constituting the endocuticle middle layer (Figure 1 in the main text).

Lakshminath Kundanati, Stefano Signetti, Himadri S. Gupta, Michele Menegon and Nicola M. Pugno (2018) Multilayer Stag Beetle elytra perform better under external loading via non-symmetric bending properties *J.Roc.Soc. Interface*

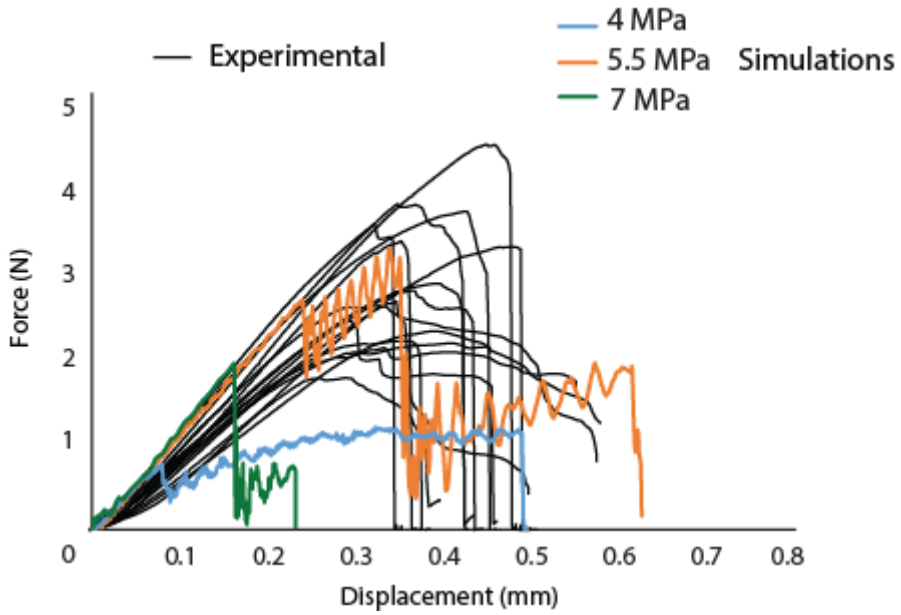

Figure S4. Comparison of bending FEM curves obtained with three different set of interface properties ($\tau_{lim} = \frac{1}{2}\sigma_{lim}$) and the experimental curves. The results suggest optimal interface strength ($\tau_{lim} = 5.5$ MPa) in the elytra.

Lakshminath Kundanati, Stefano Signetti, Himadri S. Gupta, Michele Menegon and Nicola M. Pugno (2018) Multilayer Stag Beetle elytra perform better under external loading via non-symmetric bending properties *J.Roc.Soc. Interface*

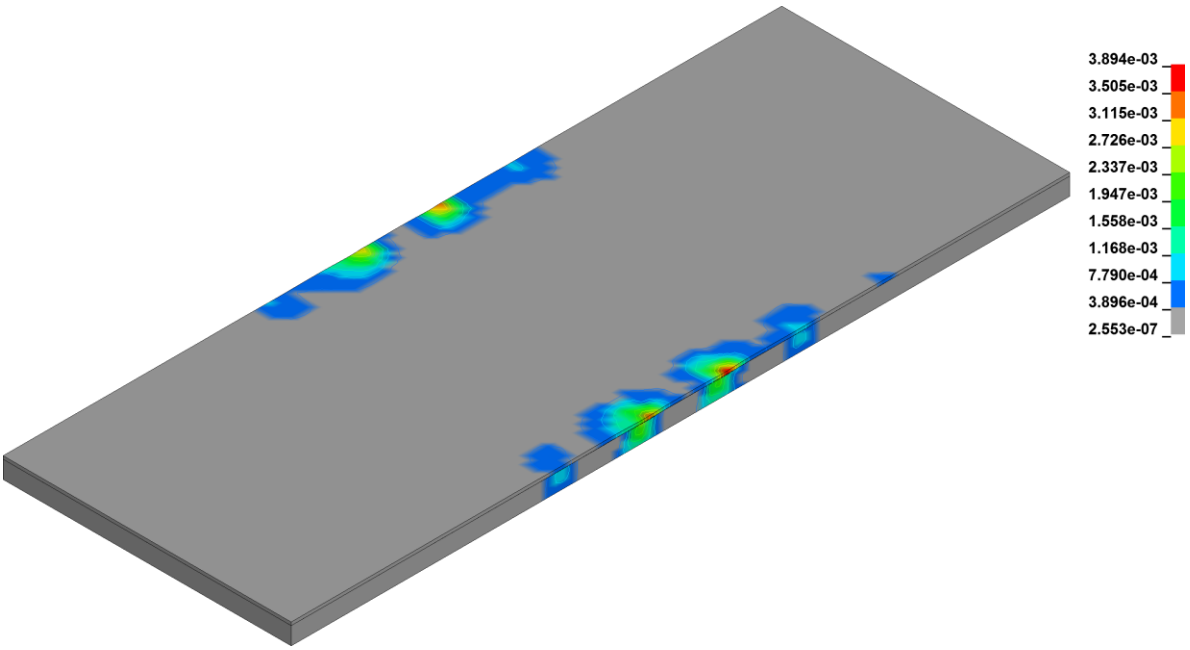

A.

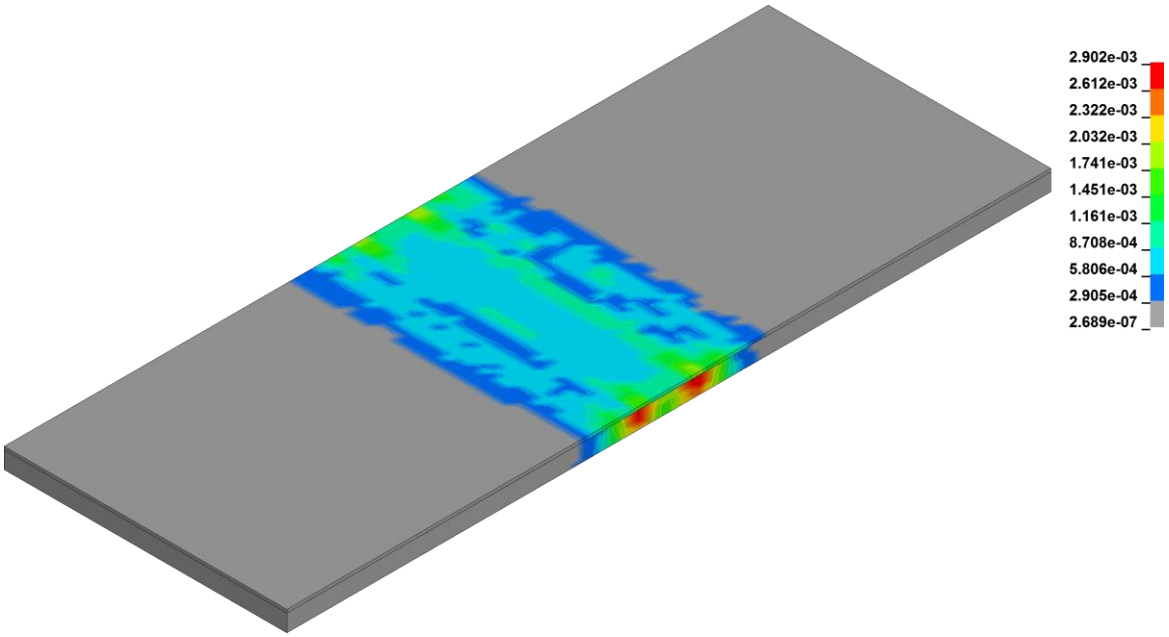

B.

Figure S5. FEM images showing the von-Mises stress distribution (unit of measure GPa) in the wing and the beetle body under a concentrated load of 0.5 N .**A)** real structure with void, **B)** elytra with no void.

Lakshminath Kundanati, Stefano Signetti, Himadri S. Gupta, Michele Menegon and Nicola M. Pugno (2018) Multilayer Stag Beetle elytra perform better under external loading via non-symmetric bending properties *J.Roc.Soc. Interface*